Radiative and Microphysical Characteristics of Deep Convective Systems in the Tropical Western Pacific

MICHAEL P. JENSEN

Columbia University/NASA Goddard Institute for Space Studies, New York, New York

ANTHONY D. DEL GENIO

NASA Goddard Institute for Space Studies, New York, New York

ABSTRACT

The radiative and microphysical characteristics of 17 precipitating systems observed by the Tropical Rainfall Measuring Mission (TRMM) satellite over Manus, Papua New Guinea, and Nauru Island are modeled. These cases represent both deep and midlevel convection. Reflectivity data from the TRMM precipitation radar and Geostationary Meteorological Satellite infrared radiometer measurements are used to parameterize the three-dimensional cloud microphysics of each precipitating cloud system. These parameterized cloud properties are used as input for a two-stream radiative transfer model. Comparisons with measurements of broadband radiative fluxes at the top of atmosphere and the surface show agreement to within 20%. In cases in which the convective available potential energy (CAPE) is large, deep convective clouds with extended anvil decks form, containing layers of ice crystals that are too small to be detected by the TRMM radar but have a large optical thickness. This results in maximum shortwave heating and longwave cooling near cloud top at heights of 12–14 km. When CAPE is small, convective clouds extend only to midlevels (4–7 km), and there are no cloud layers below the detectability limit of the TRMM radar. Radiative heating and cooling in these cases are maximum near the freezing level. A sensitivity analysis suggests that the small ice crystals near the cloud top and larger precipitation-sized particles play equally significant roles in producing the high albedos of tropical anvil clouds. A comparison of the radiative heating profiles calculated in this study with latent heating profiles from previous studies shows that for cases of mature deep convection near local solar noon, the maximum radiative heating is 10%–30% of the magnitude of the maximum latent heating.

1. Introduction

Deep convection and its associated anvil outflow cause a large perturbation in the radiation budget by increasing the shortwave albedo and reducing the infrared emission to space over timescales of one to several days and spatial scales on the order of the size of a general circulation model (GCM) grid box. These cloud systems affect the local radiative heating profile through shortwave heating near cloud top, longwave cooling near cloud top, and longwave warming near cloud base. They also cause a large surface shortwave and longwave cloud forcing. Both large and small ice crystals contribute to the radiative impact of these clouds (McFarquhar and Heymsfield 1996), but the relative amounts of small and large particles under different conditions are not well known.

The role of convective cloud systems in cloud radiative feedback and how it will change as climate changes have recently come under scrutiny. Ramanathan and Collins (1991) suggest that deep convective clouds and anvils act as a "thermostat" for tropical ocean temperatures. As the sea surface temperature (SST) increases, deep convective activity increases, resulting in more anvil outflow with greater optical thickness. This increases the cloud albedo which, in turn, decreases the solar energy absorbed by the ocean surface, regulating sea surface temperatures. More recently, Lindzen et al. (2001) suggest that warmer SSTs result in more efficient conversion of growing droplets to precipitation-sized particles in deep convection, resulting in greater rainfall and subsequently less cloudiness associated with these systems. These differing views of deep convective cloud feedback in the Tropics raise the need for a more complete understanding of these cloud systems and their radiative impacts.

In this paper we model the radiative properties of several tropical convective anvil systems, using satellite-based observations to describe the cloud and precipitation properties. The modeled radiation fields are compared with observations at the surface and the top

Corresponding author address: Dr. Michael P. Jensen, Columbia University, Armstrong Hall, 2880 Broadway, New York, NY 10025. E-mail: mjensen@giss.nasa.gov

of atmosphere (TOA) and related environmental and cloud characteristics. In section 2 of this paper the data sources are described. Section 3 describes the methods used in this study, including the parameterization of cloud and precipitation properties, the radiative transfer model and the case studies investigated. In section 4, the sensitivity of the modeled fluxes to assumptions in the cloud and precipitation parameterizations is described. Section 5 presents the calculated broadband heating rate profiles and discusses their implications. Section 6 summarizes the conclusions of this study.

2. Data

a. Tropical Rainfall Measuring Mission (TRMM)

TRMM is a satellite mission jointly conducted by the National Aeronautics and Space Administration (NASA) and the National Space Development Agency (NASDA) of Japan. The main emphasis of this mission is the monitoring and study of tropical rainfall and the associated latent energy release on climatological timescales. Of secondary importance to the goals of the mission, but of comparable importance to the tropical climate, is the study of the radiative and cloud characteristics of tropical convective systems. The TRMM satellite was launched in November 1997 with a payload (Kummerow et al. 1998) including the first spaceborne precipitation radar (PR), a passive microwave sensor, a visible and infrared scanner, the Clouds and the Earth's Radiant Energy System (CERES) (Wielicki et al. 1996), which measures TOA longwave and shortwave radiances, and the Lightning Imaging Sensor (LIS) (Christian et al. 1999), which detects and locates lightning.

In this study we use radar reflectivity data from the PR to identify precipitating convective systems and parameterize their ice/liquid water content (I/LWC). The PR has a horizontal resolution at the surface of approximately 4 km and a swath width of 220 km with a vertical resolution of approximately 250 m. It, therefore, provides an instantaneous three-dimensional (3D) snapshot of convective system structure. The I/LWC profiles derived from the PR data are used as inputs to a radiative transfer model, which calculates broadband radiative fluxes and heating rate profiles. We compare modeled radiative fluxes at the TOA to the CERES standard data product ES-8, which contains ERBE (Earth Radiation Budget Experiment)-like instantaneous TOA fluxes. The CERES instrument measures upward radiance in three different channels: shortwave (0.3–5 μm), water vapor window (8–12 μm), and total (0.3 to >100 μm), with a horizontal spatial resolution of 10 km. These radiances are then converted to instantaneous radiative flux estimates at the TOA for each CERES field of view as part of the ES-8 data product.

b. Atmospheric Radiation Measurement (ARM) Program

The ARM Program was created in 1989 with a main focus on improving the performance of general circulation models used in climate studies (Stokes and Schwartz 1994). In order to do this, ARM established several field-monitoring sites that record continuous measurements of surface radiation, clouds, atmospheric state, and surface meteorological data over climatological timescales. The locations of these sites have been chosen to represent a variety of climatic regimes and address the radiative energy balance in strategic areas of the globe. The tropical western Pacific (TWP) ARM site at Manus, Papua New Guinea (2.058°S, 147.425°E) (Mather et al. 1998), has been operational since October 1996, and the second site at Nauru Island (0.53°S, 166.92°E) began operations in November 1998. Diabatic heating associated with clouds and precipitation in the tropical western Pacific region is an important driving mechanism for the general circulation (Hartmann et al. 1984). For this study we employ ARM continuous measurements of the downwelling broadband shortwave flux. Broadband solar (280–2950 nm) fluxes are measured by Epply thermopile detector pyranometers, which provide 1-min averages of the flux within ±5% or ±10 W m^{-2} (Mather et al. 1998). The ARM suite of instruments also includes a 35-GHz millimeter cloud radar (MMCR) specifically designed to observe the small hydrometeors that compose clouds. We also use daily radiosonde profiles of temperature and humidity as input to a radiative transfer model and Geostationary Meteorological Satellite (GMS) IR images of the TWP sites and surrounding region to locate convective cloud tops.

3. Methods and analysis

We use a combination of remote sensing observations to parameterize the 3D water content of a deep convective system and its associated anvil outflow. We assume that the hydrometeors obey a lognormal size distribution (Ackerman et al. 1988) whose parameters depend on temperature and radar reflectivity. These hydrometeor size distributions are then used as input to a radiative transfer model. The calculated fluxes are then compared with measurements from CERES at the TOA and ARM at the surface. The parameterizations and model are described below.

a. Model description

In order to describe the 3D I/LWC structure of the deep convective system, we parameterize the I/LWC as a function of the equivalent radar reflectivity factor Z_e from the TRMM PR. For heights below the freezing level, we employ a parameterization of raindrop liquid contents based on the Marshall–Palmer (Marshall and

Palmer 1948) distribution with LWC $= 0.004Z_e^{0.55}$ and a mean diameter of $D_m = 1500$ μm. Use of the equivalent radar reflectivity factor Z_e contains the underlying assumption that the scatterers in the radar volume are liquid drops that are small in comparison with the wavelength. In cases in which the scattering particles are more likely composed of ice particles, we use the ice equivalent radar reflectivity factor given by

$$Z_i = (K_w^2/K_i^2)Z_e$$

(Smith 1984), where K_w (K_i) is the dielectric constant for liquid (ice) water. For the TRMM PR wavelength, a value of $(K_w^2/K_i^2) = 5.28$ is used. When the height is greater than the freezing level, two separate regimes are parameterized. For PR radar reflectivity $dBZ_e > 29$, we assume IWC $= 0.001Z_I^{0.96}$ with $D_m = 200$ μm, and for $dBZ_e \geq 29$ an upper limit of IWC $= 2.5$ g m^{-3} is used. These parameterizations were derived for tropical island–based deep convection during the Maritime Continent Thunderstorm Experiment (MCTEX) (Jensen et al. 2002).

The resulting 3D representation of the hydrometeor size distributions is then used as input to a two-stream radiative transfer model (Toon et al. 1989). This model uses a correlated-k technique for absorption by atmospheric constituents (Kato et al. 1999) for 26 bands in the solar spectrum from 0.25 to 4.5 μm and 18 bands in the IR from 4.8 to 35.8 μm. The profiles of temperature and water vapor are taken from the nearest sounding preceding the TRMM overflight time. The model uses Mie scattering theory to calculate the single scattering properties of cloud and precipitation hydrometeors. Previous studies conclude that Mie theory is not appropriate for calculating single scattering properties of ice crystals, specifically, the asymmetry parameter that has a mean value of $g = 0.89$ for Mie calculations should have a value nearer $g = 0.7$ (Stephens et al. 1990; Francis et al. 1994). We use the Mie-calculated scattering properties except for the asymmetry parameter, which is set to 0.7 for all solar wavelengths. We use an independent pixel approximation (IPA) (Cahalan et al. 1994); that is, we treat each column as plane parallel and homogeneous and neglect interactions between columns. The vertical resolution is identical to the 250-m PR resolution. The result is a 3D field of modeled upwelling and downwelling fluxes and heating rates for each column and model level.

b. Case study—20 June 1998, Manus Island

At 0259 UTC 20 June 1998 (1248 LT), the TRMM satellite ground track was within 40 km of the Manus ARM site. At this time the TRMM satellite observes a portion of a mature cloud merger over Manus, which includes deep convective core regions, connecting stratiform regions, and a large cirrus anvil. Convective core regions are identified as areas that lack a radar bright band and show surface rain rates, as determined by the

TRMM PR rainfall algorithm (TRMM data product 2A23), in excess of 100 mm h^{-1}. Stratiform regions have a clearly defined radar bright band and much lower rain rates. Figure 1 shows a set of four GMS infrared images (0131–0431 UTC) of this region with the location of the ARM Manus site indicated by the "M." The IR brightness temperatures are less than 200 K in the strongest convective towers and increase farther away. The main convective area moves from east to west over the Manus site, such that the convective towers are directly over the site at 0131 and 0231 UTC. At the time of the TRMM overflight, the convective region has moved to the west of the island with a stratiform rain region extending over the site. The IR brightness temperature over the Manus site at the time of the TRMM overflight is 205 K. We observed very high visible albedo, ranging between 0.65 and 0.75, over much of the cloud area, the highest albedos being located near embedded convective towers. Figure 2 shows the TRMM radar echo-top height. Three separate convective towers are evident in the Manus region. These areas, where the TRMM radar detects higher echoes than neighboring areas, are located at (3.0°S, 146.6°E), (3.1°S, 147°E), and (1.5°S, 148°E), and have echo-top heights of 14–16 km.

The collocation of the observations from the TRMM satellite allows us to compare the radiative fluxes modeled from the PR observations with the flux observations from the CERES instrument. Figure 3 shows a comparison of the TOA-modeled broadband shortwave and longwave fluxes and measurements from CERES. For this comparison, we assume that the radiative fluxes do not vary on scales smaller than the CERES data product (10 km). Each calculated radiative flux is compared with the nearest CERES measurement. This comparison shows a rather poor agreement between the measured and modeled fluxes. Upwelling shortwave fluxes at the TOA are generally greater than the modeled fluxes with a mean difference of 56.1% $\pm$ 28.3%. Likewise, the modeled upwelling longwave flux shows poor agreement with observations, with a mean difference of 104% $\pm$ 30.5%. These large discrepancies are due to the role of cloud particles that are not detected by the TRMM PR.

The TRMM PR is not designed to detect small cloud particles, and, thus, the radar-detected cloud top is, in general, not the actual cloud top. In order to account for the small-particle cloud-ice near the top of the anvil complex, we have derived a simple linear relationship between the temperature and ice water content using MMCR reflectivity measurements and radiosonde temperature profiles. The ARM MMCR on Manus has been operational since June 1999. Because data are not available for the 20 June 1998 case, we search for TRMM observations of the edges of anvil systems over Manus Island. For the cases we have identified, only one satisfies the criteria of including MMCR observations of the edge of the anvil complex (000525). The left-hand
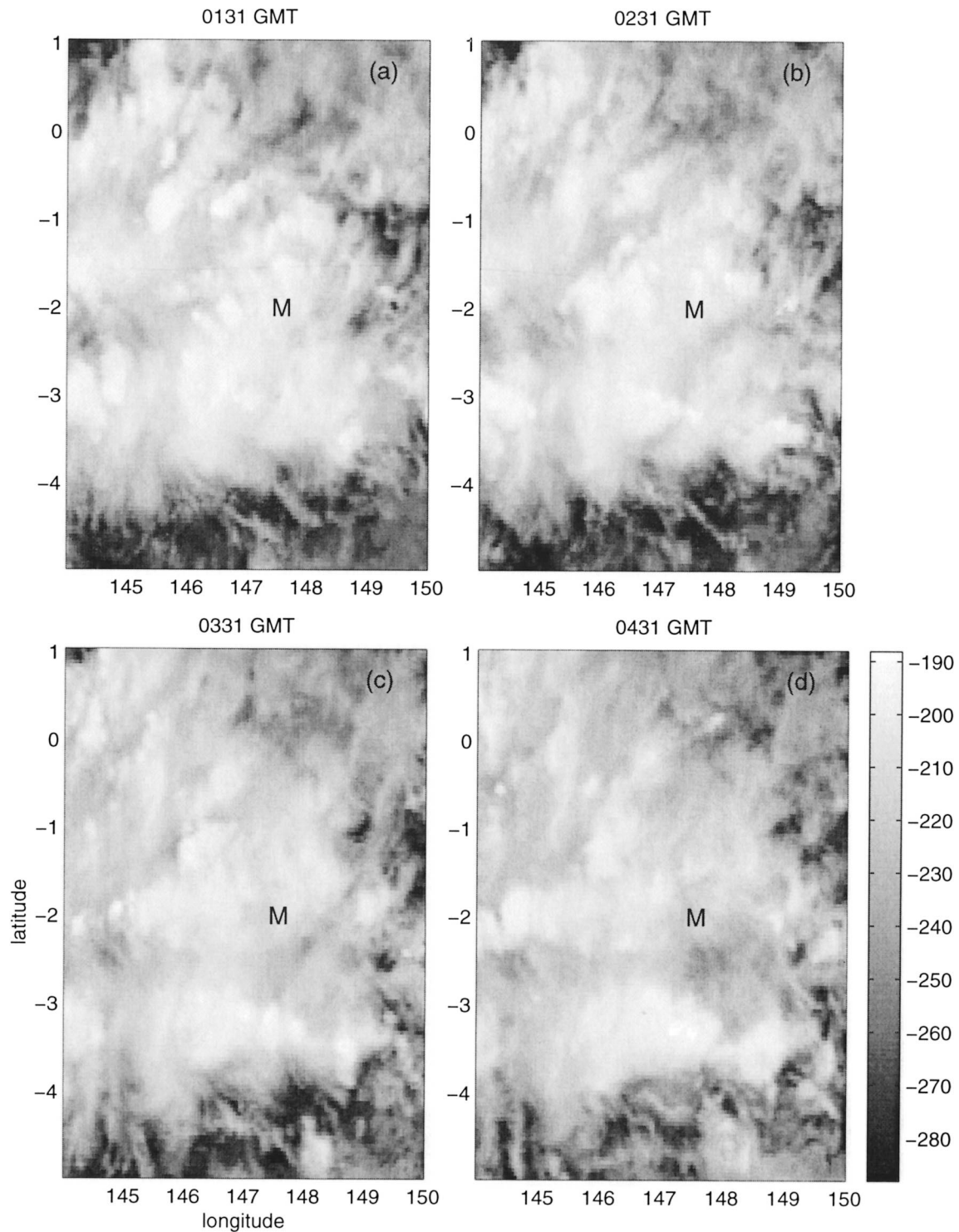
FIG. 1. GMS IR brightness temperature (K) for (a) 0131, (b) 0231, (c) 0331, and (d) 0431 UTC 20 Jun 1998. The location of the Manus ARM site is indicated by the M.

panel of Fig. 4 shows the MMCR radar reflectivity factor for 25 May 2000. Also noted in the figure are the IR equivalent cloud-top height (X) for each GMS satellite image, the time of the TRMM overflight (vertical line), and the echo-top height observed by the TRMM PR (O). The right panel of Fig. 4 shows the TRMM PR radar reflectivity profile for Manus at the time of the overflight.
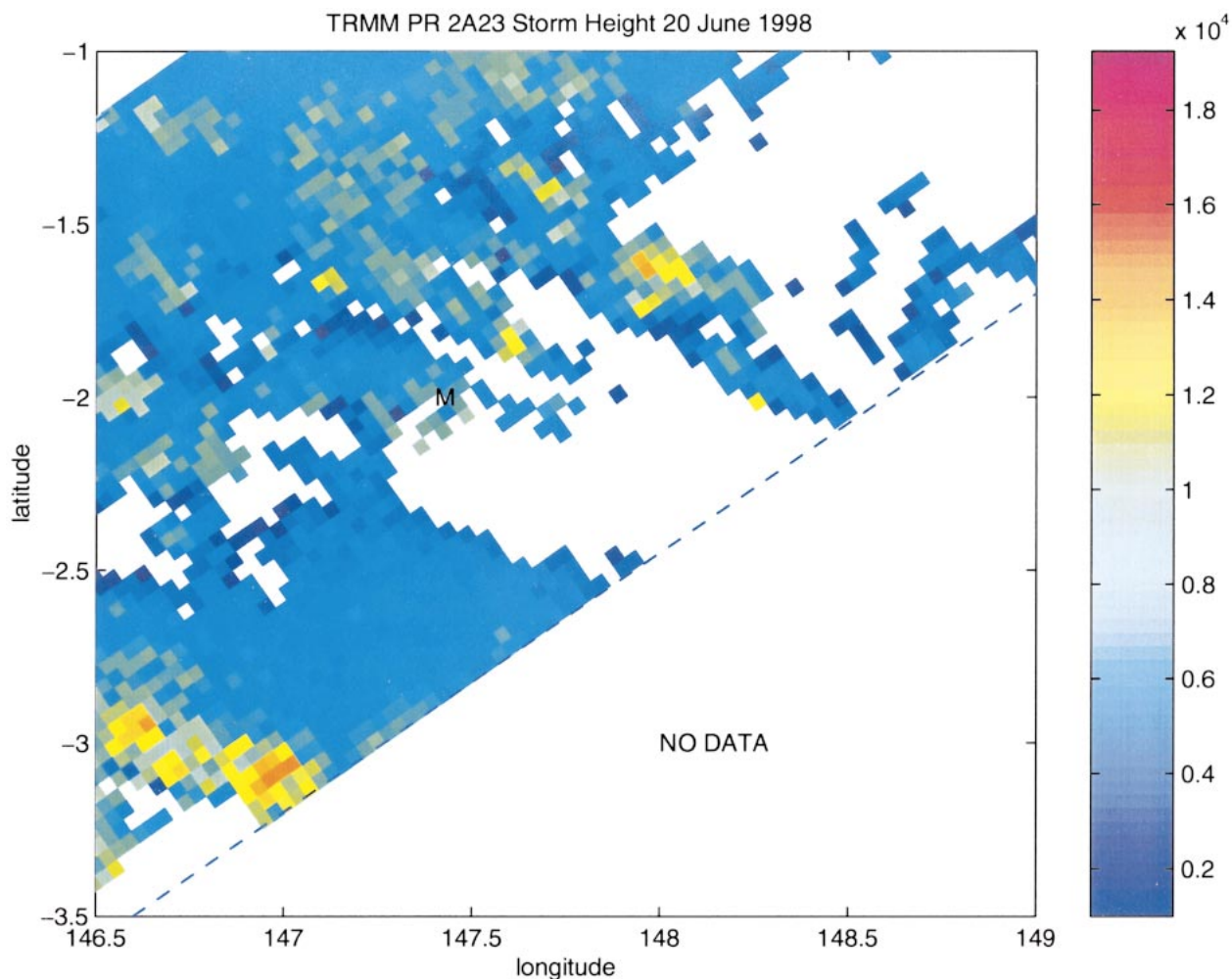
FIG. 2. TRMM PR echo-top height (m) for 0259 UTC 20 Jun 1998. The location of the Manus ARM site is indicated by the M.

We use the MMCR reflectivity to parameterize the IWC and assume a simple quantized linear relationship between temperature and particle size (Table 1), based on in situ aircraft observations by Heymsfield and McFarquhar (1996) during the Central Equatorial Pacific Experiment (CEPEX). These cloud microphysical properties are used as input to the radiative transfer model described above. We tried several different IWC $= aZ_i^b$ parameterizations, including two from Heymsfield and Palmer (1986) and one from Jensen et al. (2002). For each model run, using a different parameterization, we compare the modeled downwelling shortwave flux at the surface with the surface radiometer observations. Figure 5 shows the results of two of these model runs. The closest fit between the model and observation data was obtained when using the Jensen et al. (2002) parameterization, IWC $= 0.5Z_i^{0.36}$. We linearly decrease this IWC by multiplying by ϵ, which decreases from 1 by steps of 0.01 until the fit between modeled and measured fluxes is a minimum ($\epsilon = 0.5$). We use

the parameterized values of IWC $= 0.5(0.5Z_i^{0.36})$ for the anvils in the Manus region.

Figure 6 shows the mean IWC at each radar range gate level plotted as a function of temperature from the nearest sounding. The results show a linear trend with a least squares fit of IWC (g m^{-3}) $= 0.0032T$ (°C) $+ 0.3135$. We use this relationship to describe the IWC between the top of the radar echo and the IR equivalent cloud-top height. The IR equivalent cloud-top height is defined as the height of the environmental temperature that matches the GMS IR brightness temperature, a good estimate for the optically thick clouds that are our focus.

Figure 7 is similar to Fig. 3, but now compares the CERES-observed fluxes with the modeled flux using the derived relationship for IWC in the region between the TRMM echo-top height and the IR equivalent cloud-top height. This figure shows that the TOA upwelling shortwave fluxes generally agree to better than 10% with a mean of 1% $\pm$ 9.6%. For longwave fluxes this agreement is also quite good, with a mean of $-2.9\% \pm 5.3\%$.

[(model SW) − (CERES SW)]/CERES SW

NO DATA

mean = −56.1 %

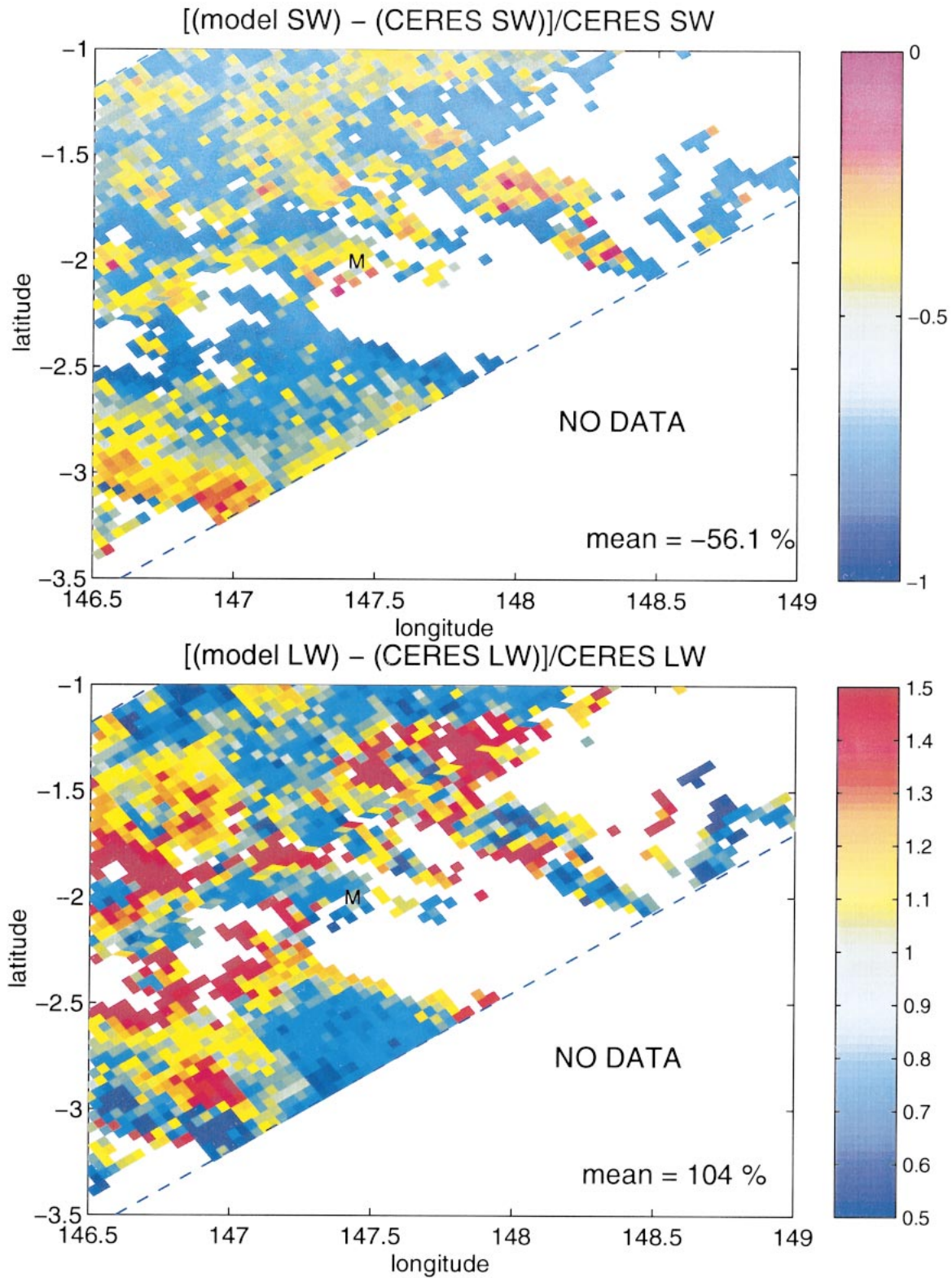[(model LW) − (CERES LW)]/CERES LW

NO DATA

mean = 104 %

FIG. 3. Comparison of the modeled upwelling broadband shortwave radiation at the TOA and observations from the CERES instrument aboard the TRMM satellite for the 20 Jun 1998 deep convective case using only TRMM PR data to parameterize the cloud microphysics.
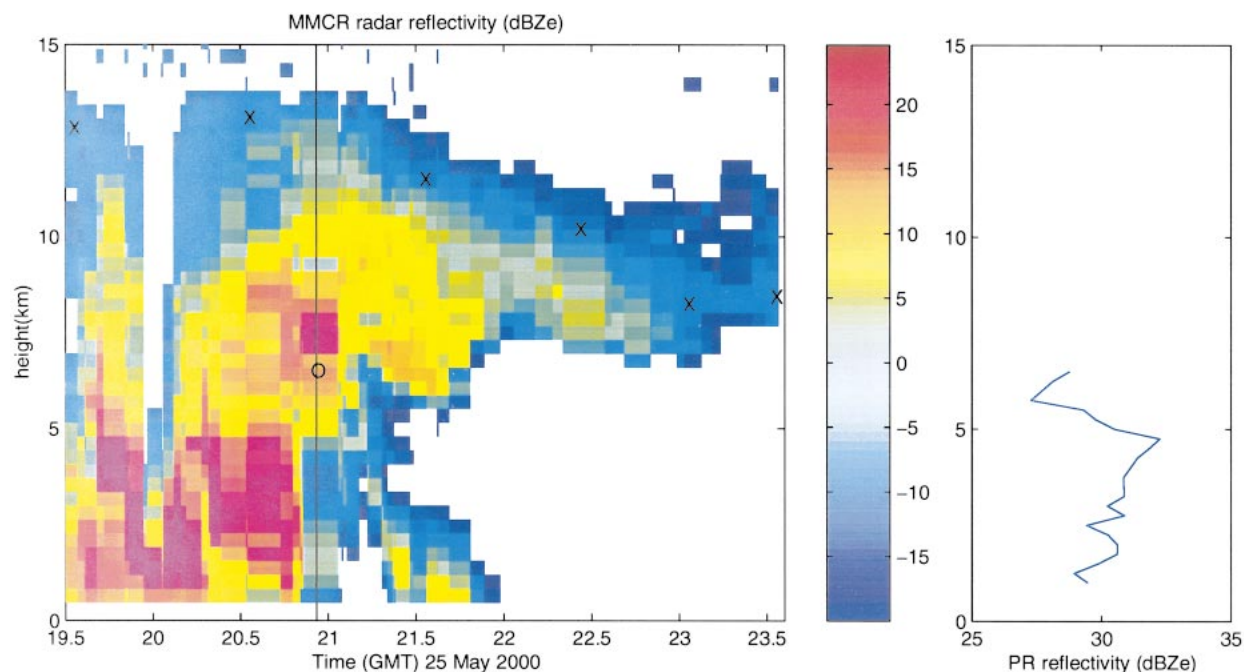
FIG. 4. (left) The 35-GHz millimeter cloud radar reflectivity at Manus Island on 25 May 2002. The hourly GMS IR equivalent cloud-top heights are indicated by the Xs. The vertical line indicates the time of the TRMM satellite overflight, with the TRMM PR storm height indicated by the O. (right) The TRMM PR reflectivity profile over the Manus ARM site.

Some large discrepancies are seen near precipitation region edges, where the IPA breaks down, and differences in CERES and TRMM resolution result in poor comparisons. This agreement to within 10% is slightly better than previous studies (Jensen et al. 2002) of deep convective systems during MCTEX. These errors are attributed to uncertainties in the parameterization of the hydrometeor size distributions and to limitations in the IPA.

c. Case study—9 February 1998

At 2225 UTC February 1998 (0815 LT), the TRMM satellite ground track was within 80 km of the Manus ARM site. At this time the TRMM satellite observes a region of midlevel precipitating cloud over Manus. Figure 8 shows a set of four GMS IR images (2131–2331 UTC) of this area. This cloud system is characterized by relatively high IR brightness temperatures over Ma-

TABLE 1. Mean ice particle radius as a function of temperature, derived from data in Heymsfield and McFarquhar (1996).

Temperature (°C)	Mean radius (μm)
$T \geq -21$	220
$-31 \leq T < -21$	182
$-41 \leq T < -31$	144
$-51 \leq T < -41$	106
$-61 \leq T < -61$	68
$T < -61$	30

nus (260–270 K), the absence of a radar bright band, and a mean surface rain rate of less than 50 mm h^{-1}.

The visible albedo is much lower than the deep convective case, ranging between 0.2 and 0.45. There is a deep convective cell approximately 200 km to the southwest of Manus with IR brightness temperatures as low as 225 K; however, the much warmer cloud tops over Manus do not seem to be associated with this system. If we assume that the clouds over Manus are optically thick, then the cloud-top height is about 6 km, just above the environmental freezing level (~5.1 km). Figure 9 shows the echo-top height from the TRMM PR reflectivity measurements. The echo tops over Manus are on the order of 5 km. Note that for this case, there is a relatively small difference between the IR equivalent cloud-top height and the TRMM PR echo-top height, in comparison with the 20 June 1998 deep convective case.

Figure 10 shows a comparison of the modeled upwelling broadband fluxes at the TOA and measurements from the CERES instrument. This comparison shows that for shortwave fluxes, the model underestimates the reflected shortwave radiation with a mean of −28.8% ± 29%. These large discrepancies are most likely the result of two effects. First, the elongated shape of the precipitation area results in large underestimates of reflected shortwave radiation when compared with a precipitating pixel and large overestimates in nonprecipitating columns. This explains the large differences near 2°S, 147°E and to the south and southwest of Manus.
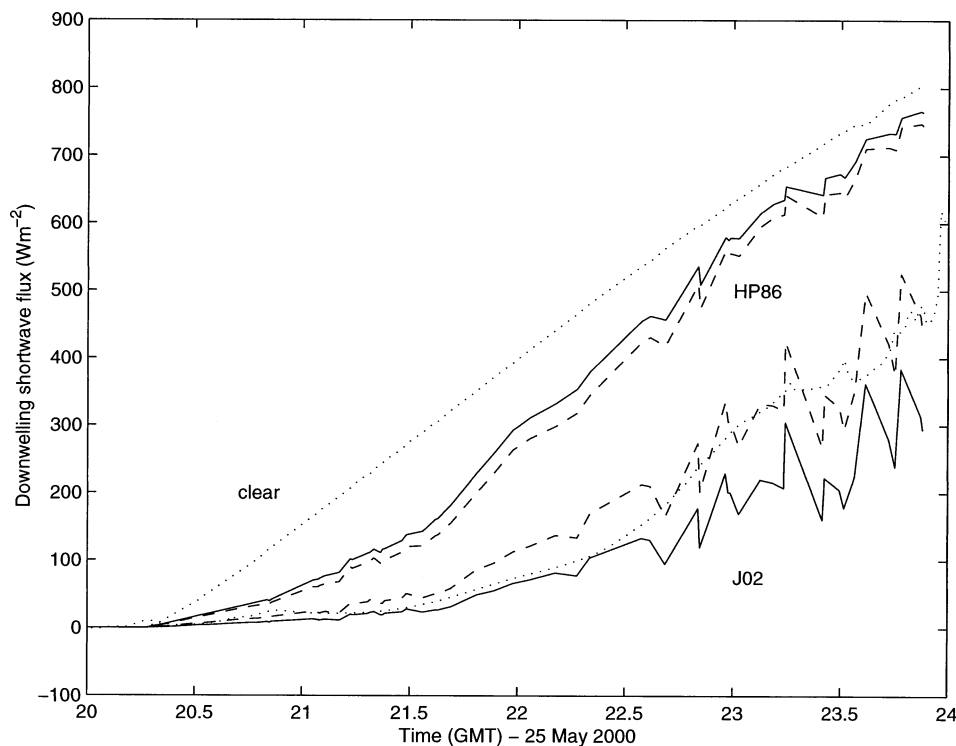
FIG. 5. Modeled broadband downwelling shortwave flux at the surface using different Z_i–IWC parameterizations. The curves use the parameterization of Jensen et al. (2002), IWC $= 0.5Z_i^{0.36}$ (J02, solid); that parameterization decreased by 50%, IWC $= 0.5(0.5Z_i^{0.36})$ (J02, dashed); the parameterization of Heymsfield and Palmer (1986), IWC $= 0.017Z_i^{0.529}$ (HP86, solid); and that parameterization increased by 50%, IWC $= 0.5(0.017Z_i^{0.529})$ (HP86, dotted). The dotted lines represent the observations and the clear-sky calculation.

Second, we expect a much larger contribution to the total optical thickness from liquid cloud droplets in these midlevel cases in comparison with the deep convective cases. The cloud liquid particles are not accounted for in our parameterizations. For longwave fluxes the agreement is much better with a mean of −7.5% ± 9.5%. The emitted longwave flux is closely tied to the total liquid water path (LWP) rather than the particle sizes. The much better agreement in the emitted longwave in comparison with reflected shortwave may indicate that the precipitation-sized particles detected by the TRMM PR represent a significant portion of the LWP compared to a smaller fraction of the total optical depth. There is also a contribution to the upwelling longwave flux at TOA from water vapor present above the cloud. This will act to offset decreased longwave emission from the cloud due to an underestimation of the LWP.

d. Additional precipitating cases

In addition to the 20 June 1998 and 9 February 1998 cases, 15 additional storms were investigated. The only criterion used in choosing these cases was that the TRMM PR detect precipitation over the Manus and Nauru ARM TWP sites during the daytime. Table 2 summarizes the date, time, location, mean radar echo-top height, and mean IR equivalent cloud-top height of all precipitating cloud systems observed simultaneously by TRMM and ARM during the time from the launch of TRMM until 31 December 2000.

In order to further characterize the 17 cases, we consider the environmental soundings and storm-averaged quantities for each case. For each of the columns containing a TRMM PR radar return for each of the 17 cases summarized in Table 2, we have constructed profiles of the microphysical properties of the cloud column using the TRMM PR reflectivity, the GMS IR brightness temperature, a set of Z–I/LWC parameterizations, and assumptions about the particle sizes and distribution shapes. The 17 cases can be divided into three distinct subsets, based on their mean radar/radiative properties and the thermodynamic environment in which they form (see Table 2). Four of the cases (980209, 980328, 990623nauru, 990726) are characterized by midlevel IR equivalent heights (<7 km) that are equal to (or in some cases even less than) the radar echo height, implying that the radar may be detecting the actual cloud-top height. Nine of the cases show relatively deep IR equivalent heights (>9 km), with as great as a 6.5-km difference between the mean radar echo-top height and the mean IR equivalent cloud-top height. The remaining four cases (980404, 990718, 990720nauru, 990726) are near edges of deep convective regions and may not be representative of the system as a whole.
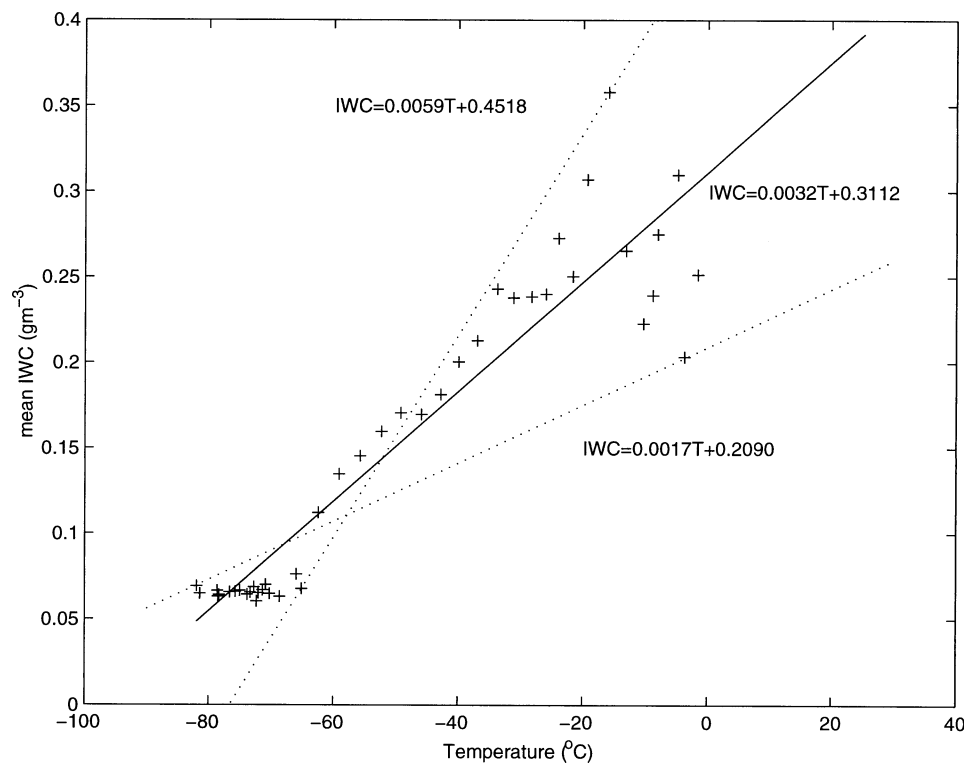
FIG. 6. Mean ice water content (g m^{-3}) as a function of temperature (°C). The least squares fit is shown (solid). Linear fits to the extreme points at high and low temperatures are also shown (dotted) for sensitivity analysis.

Figure 11 shows a comparison between the modeled and 10-min mean measured shortwave cloud forcing at the surface in the column directly over Manus (or Nauru). For 12 of the 17 cases, the modeled shortwave cloud forcing at the surface agrees with the measured shortwave cloud forcing to within 20%. In general, the model tends to underestimate shortwave reflection. Although the two cases that show the poorest agreement between modeled and measured values are midlevel cases, the calculations for the remaining two midlevel cases show rather good agreement with observations. There are several possible explanations for the observed discrepancies: 1) uncertainties in the parameterization of cloud microphysics, 2) a breakdown of the IPA due to cloud geometry, and/or 3) a neglect of cloud liquid water in the model. I/LWC have been shown to vary depending on factors such as location, type of storm, and dynamics of the storm (Sassen 1987; Sauvageot 1992). The parameterizations for IWC used in this study are taken from Jensen et al. (2002) and were developed for deep convective cloud systems over the Tiwi Islands, near Darwin, Australia. We assume that these parameterizations are applicable to the systems in this study, however, the deep convective systems over Manus and, especially, Nauru are more likely to be oceanic in character as compared with the island-based systems of MCTEX. Oceanic storms tend to rain more lightly and have less vigorous updrafts implying smaller ice crystals

than land storms (Del Genio and Kovari 2002). Because Z_e is sensitive to large particles, more ice mass is required to produce a given Z_e over ocean than land. A parameterization developed for continental storms, thus, probably underestimates IWC in maritime storms. The absence of any studies dealing specifically with the parameterization of I/LWC from radar reflectivity in oceanic convective systems leaves us no choice but to use the parameterization from Jensen et al. (2002). In addition, cloud-resolving model simulations matched to TRMM Microwave Imager (TMI) radiances indicate a nonnegligible contribution to optical depth from cloud liquid water (Del Genio and Kovari 2002), which is not included in our radiative transfer model.

In cases where Manus (or Nauru) lies near the edge of a cloud, or near a region of high-reflectivity gradient, it is expected that the IPA will break down and 3D radiative effects can become significant. There are four cases (990623nauru, 990720nauru, 990726, 001225) in which the model underestimated the surface shortwave cloud forcing by greater than 25% and by as much as 51%. As a simple estimate of the horizontal heterogeneity of the precipitation, we calculate the difference between the modeled cloud forcing of the pixel over Manus and the mean modeled cloud forcing of the pixels adjacent to the Manus pixel. The cases in which the largest differences between modeled and measured cloud forcing occurred were also the cases with the
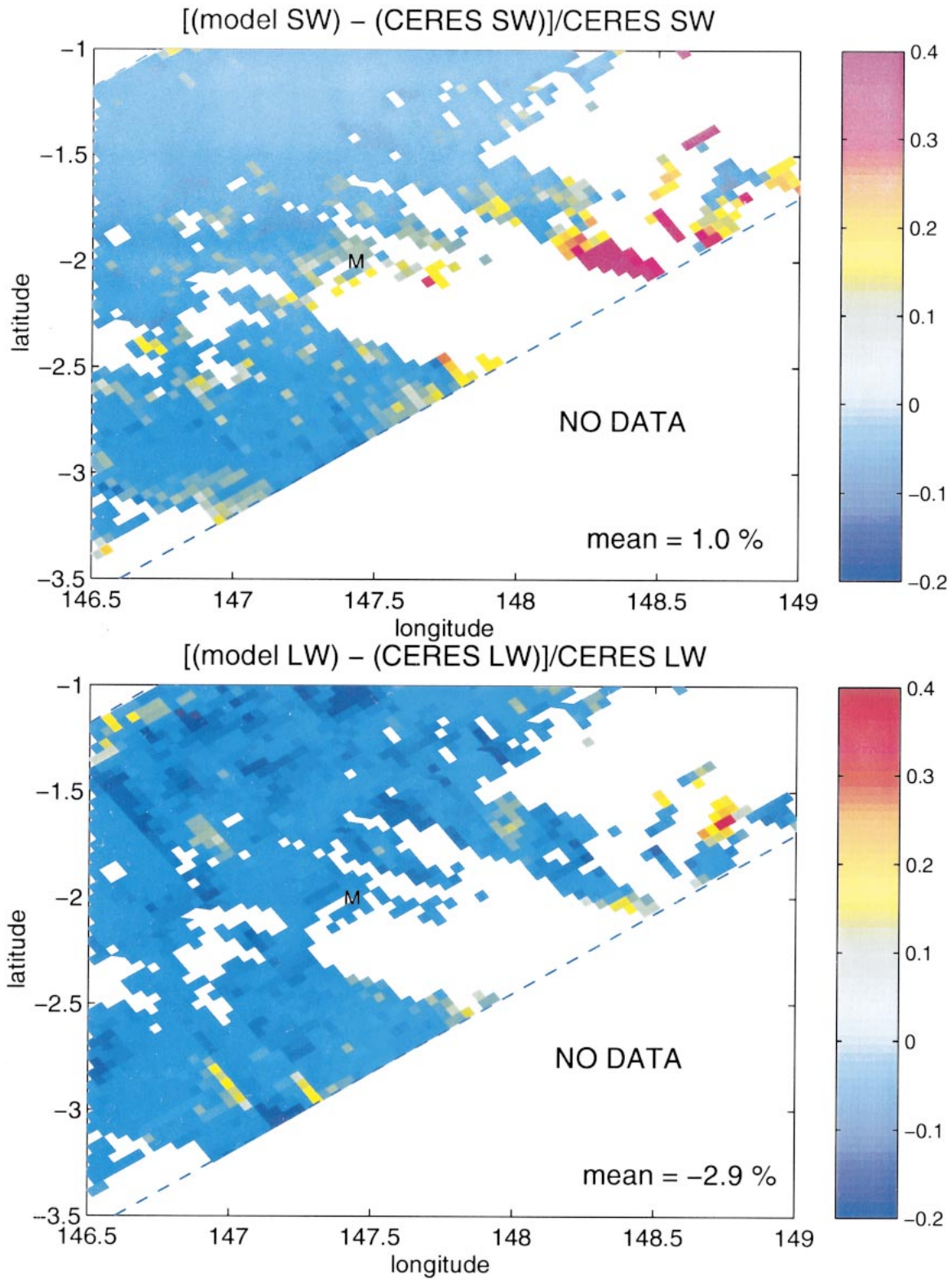
FIG. 7. Comparison of the modeled upwelling broadband shortwave radiation at the TOA and observations from the CERES instrument aboard the TRMM satellite for the 20 Jun 1998 deep convective case.
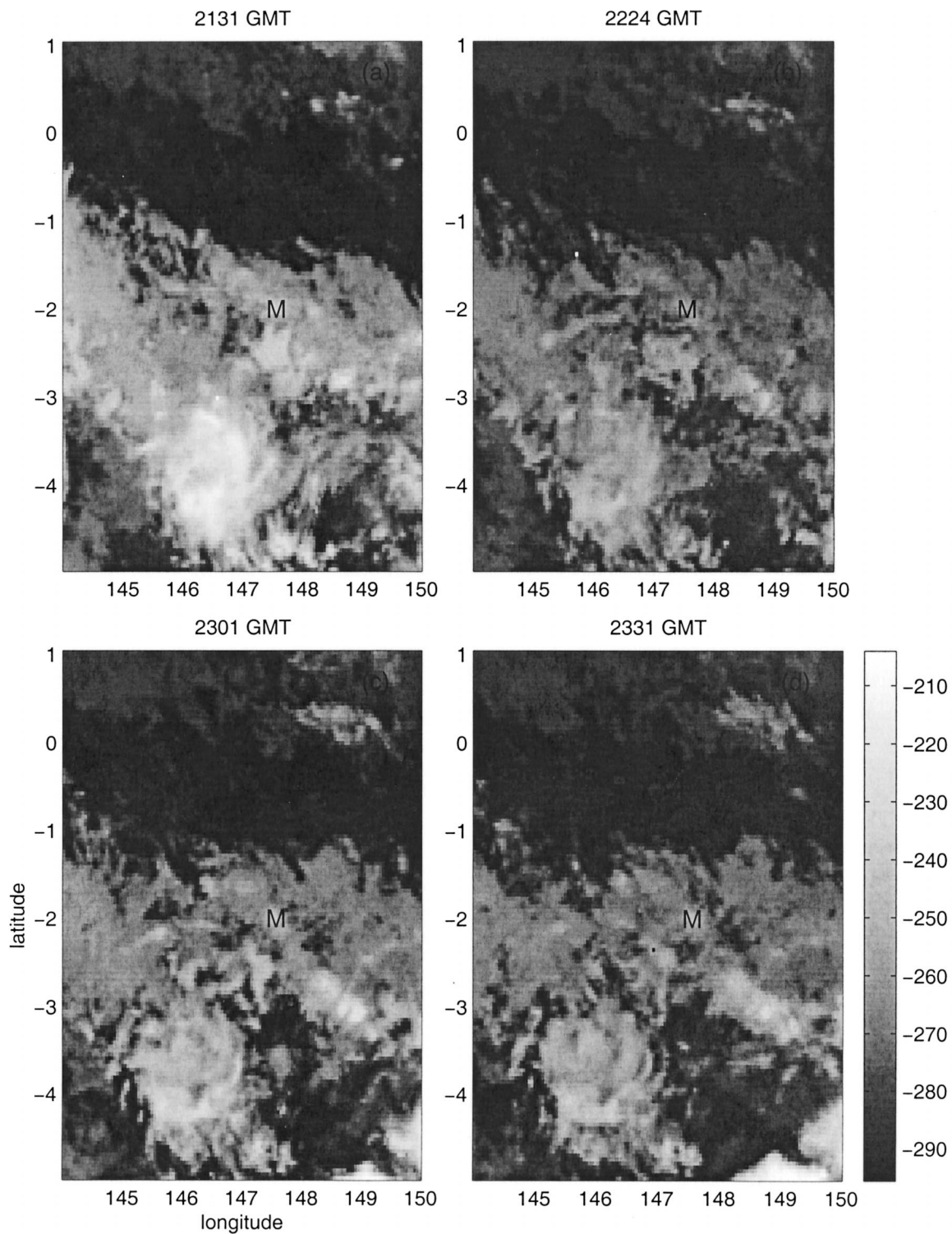
FIG. 8. GMS IR brightness temperature (K) for 2225 UTC 9 Feb 1998. The location of the Manus ARM site is indicated by the M.

greatest cloud heterogeneity. Inspection of the GMS IR equivalent heights and TRMM PR reflectivity indicates that these are cases of midlevel convection in which Manus (or Nauru) is near the edge of the precipitation region. Despite these uncertainties in comparisons at a single column we find that, although cloud inhomogeneity can result in differences on the order of 10% in the measured fluxes, the modeled values generally agree
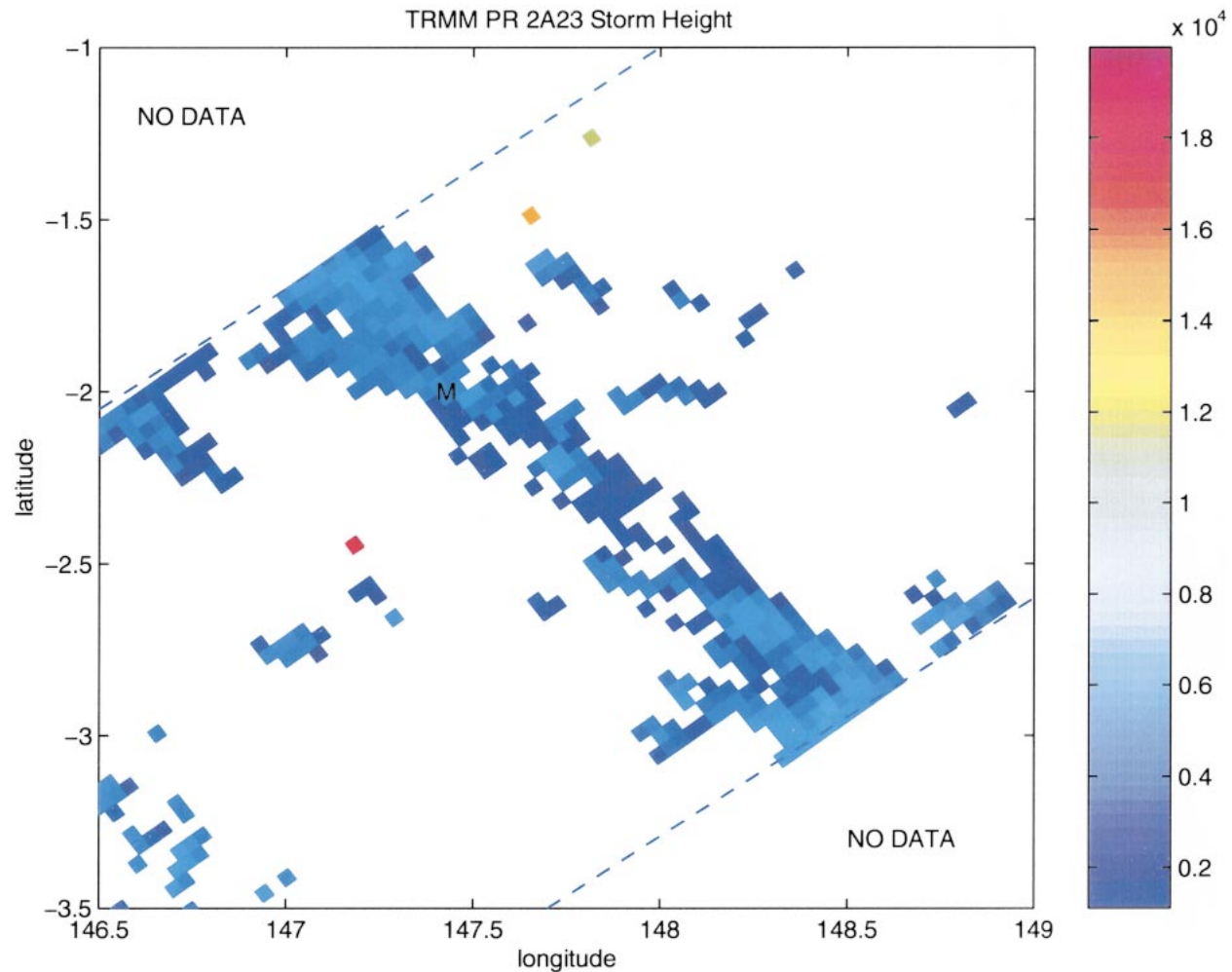
FIG. 9. TRMM PR echo-top height (m) for 2225 UTC 9 Feb 1998. The location of the Manus ARM site is indicated by the M.

to within 20%, consistent with previous studies (Jensen et al. 2002; Churchill 1992).

In order to gain more insights into the differences between these categories, we calculated the convective available potential energy (CAPE) from a sounding preceding each of the observations. Each sounding is subject to a rigorous data quality procedure by the ARM instrument mentor, including visual inspection and a comparison with microwave radiometer–integrated water path observations. The CAPE is calculated, as defined by Moncrieff and Green (1972),

$$CAPE = \int g[(\theta_{v,p} - \theta_{v,env})/\theta_{v,env}]\, dz,$$

where g is the accelerations of gravity, $\theta_{v,p}$ is the virtual potential temperature of a parcel that is lifted from the surface, $\theta_{v,env}$ is the virtual potential temperature of the environmental sounding, and the integration is taken from the level of free convection to the equilibrium level of the surface parcel.

Semilog plots of combinations of the CAPE, mean difference between the radar echo top and the IR equivalent cloud-top height, the storm-averaged modeled cloud forcing, and the storm-averaged GMS visible albedo are shown in Fig. 12. Although a greater number of cases are needed to make statistically significant conclusions from these plots, some comments on the general trends are warranted. In general, as the environmental CAPE increases, the mean difference between radar echo top and IR equivalent height increases (Fig. 12, upper left). There are three outliers (h, p, q) on this plot for which GMS imagery indicates that at the time of the TRMM overflight these cloud systems were in an early growth phase and not yet at their mature phase. As a storm evolves, we might expect CAPE to be consumed while the cloud develops vertically and large ice crystals sediment, which would imply a migration up and to the left of Fig. 12a over the life cycle of the deep convective system. There is also a general increase in the modeled cloud forcing as the CAPE increases (with the same three outliers and explanations; Fig. 12, upper
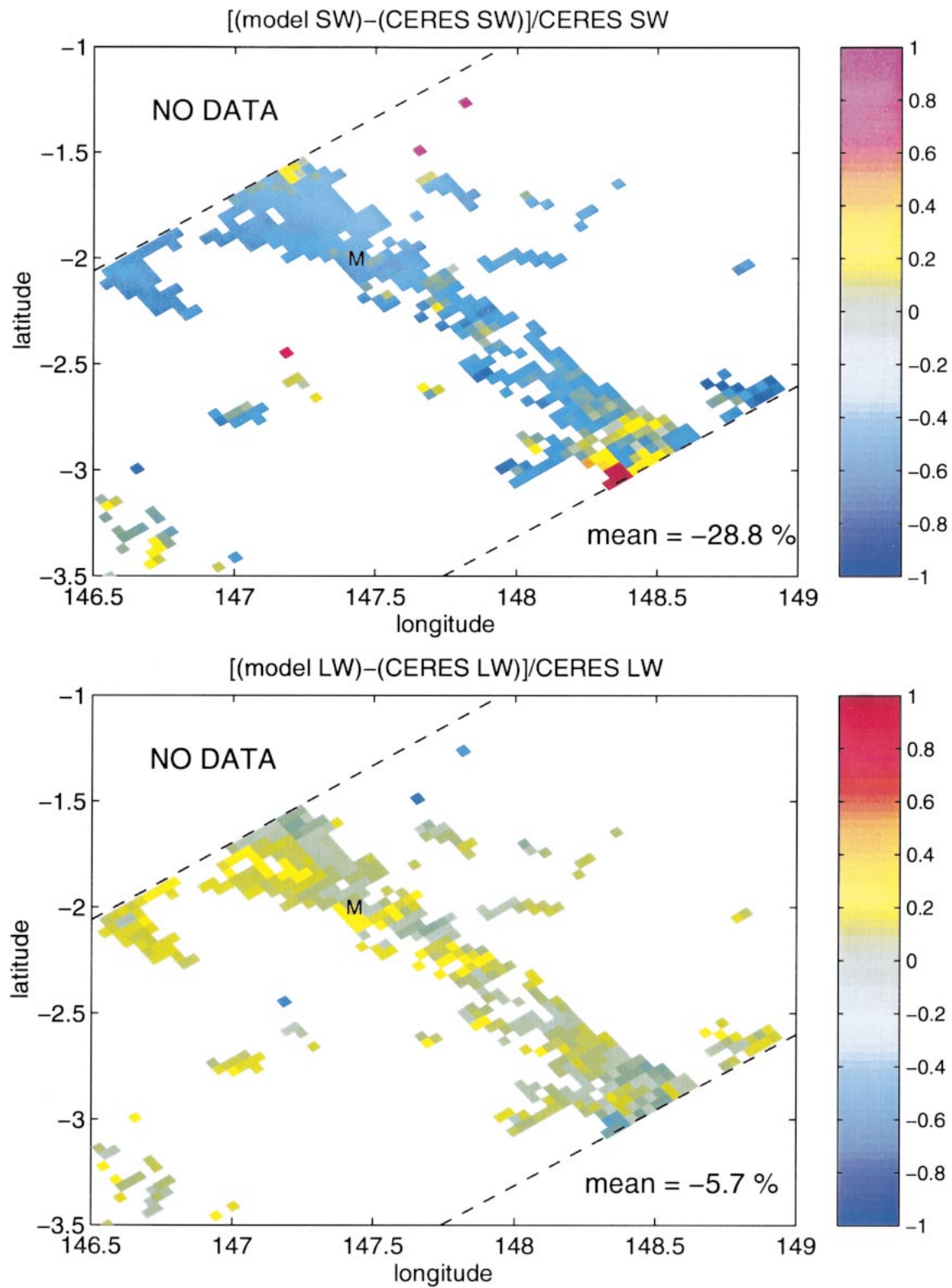
FIG. 10. Comparison of the modeled upwelling broadband shortwave radiation at the TOA and observations from the CERES instrument aboard the TRMM satellite for the 9 Feb 1998 midlevel convective case.

TABLE 2. Date, time (UTC), location, mean radar echo-top height, and IR equivalent cloud-top height of all cases during the time from the launch of TRMM until 21 Dec 2000 in which the TRMM PR observed precipitation in the column over the Manus or Nauru Island ARM sites.

Case	Date (19/20YYMMDD)	Time (UTC)	Location	Radar echo-top height (km)	IR equivalent cloud-top height (km)
a	980209	2225	Manus	5.1	6.0
b	980328	2211	Manus	6.1	6.7
c	980404	0710	Manus	5.8	10.0
d	980620	0259	Manus	8.2	14.3
e	981203	0131	Manus	7.5	12.8
f	990209	0132	Manus	6.5	10.2
g	990718	0326	Manus	6.6	9.0
h	990726	2259	Manus	5.3	5.3
i	000525	2056	Manus	7.2	9.8
j	000601	0554	Manus	6.5	11.7
k	000624	0534	Manus	7.4	12.3
l	000825	2116	Manus	6.4	11.5
m	001130	0725	Manus	7.0	12.1
n	001215	2320	Manus	6.6	10.2
o	001225	0617	Manus	6.2	10.7
p	990623	0301	Nauru	6.1	4.3
q	990720	0105	Nauru	6.2	8.2

right). For the lower two panels of Fig. 12, midlevel cases and cases near sunrise and sunset are removed. The albedo generally increases with both increasing radar echo-top height and an increase in the difference between the radar echo-top height and the IR equivalent cloud-top height (a proxy for the amount of small ice crystals). A comparison of the radar echo-top height and IR equivalent cloud-top height (not shown) indicates that as the radar echo-top height increases (i.e., the convection strengthens), the thickness of the small particle layer also increases and the shortwave albedo increases. Comparing the lower panels of Fig. 12, we
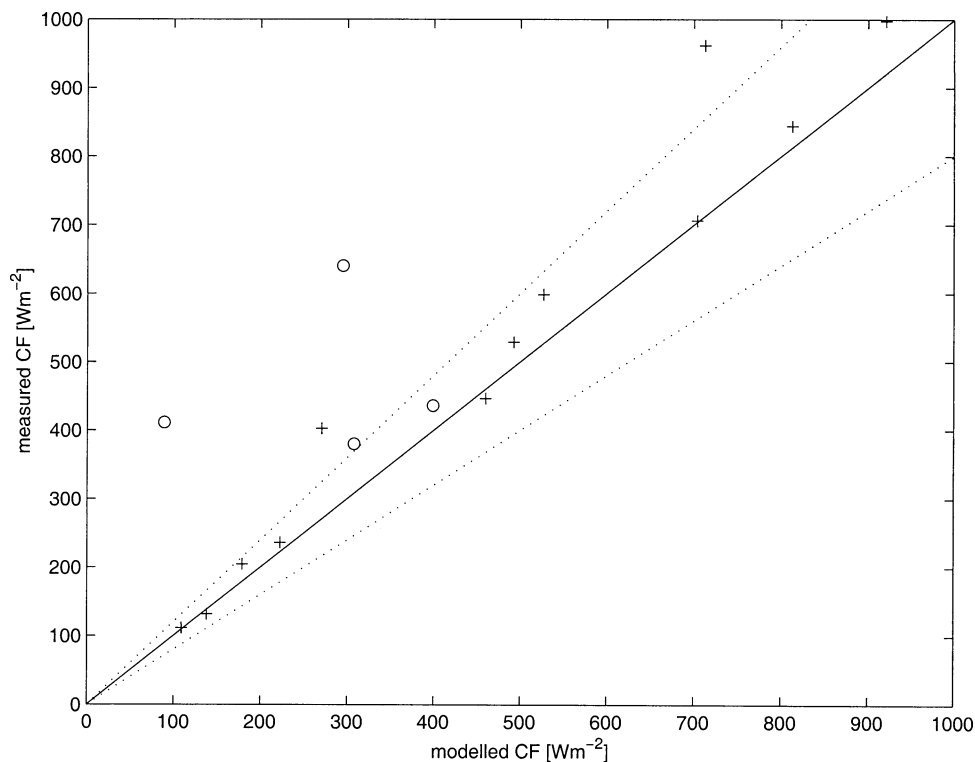

FIG. 11. Comparison of the modeled and measured shortwave cloud forcing (cloudy-sky flux subtracted from the clear-sky flux) at the surface for Manus for the 17 cases summarized in Table 2. Only cases in which precipitation was detected by the TRMM PR are included. The circles identify midlevel cases and the + indicate deep convective cases. The dotted lines represent ±20% from the $x = y$ line.
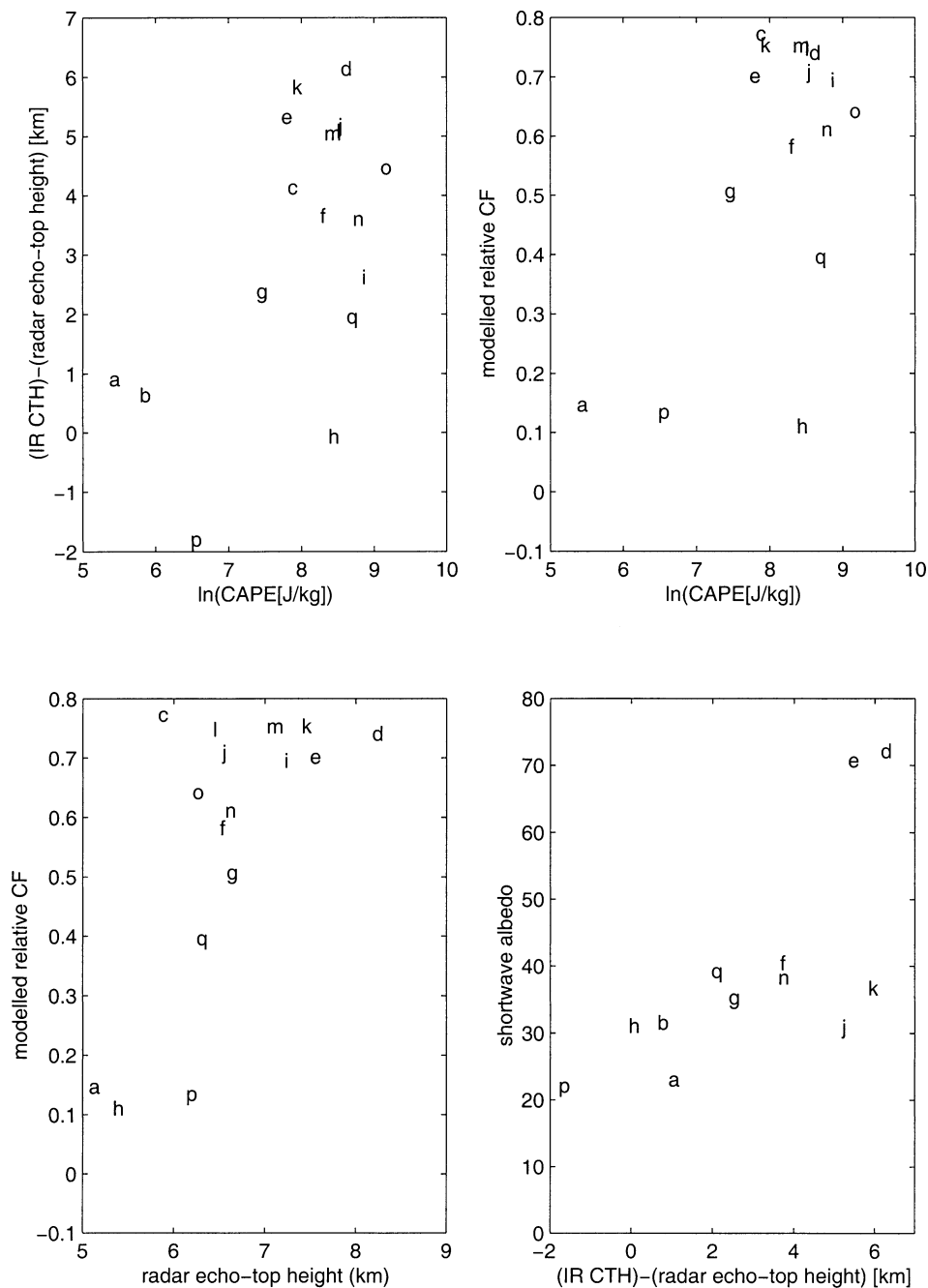
FIG. 12. Scatterplots of (top left) $\ln[\text{CAPE}(\text{J kg}^{-1})]$ vs mean difference between IR equivalent cloud-top height and radar echo-top height (km), (top right) $\ln[\text{CAPE}(\text{J kg}^{-1})]$ vs mean modeled relative solar cloud forcing at the surface, (bottom left) mean radar echo-top height (km) vs storm-averaged visible albedo, and (bottom right) mean differences between IR equivalent cloud-top height and radar echo-top height (km) vs storm averaged visible albedo at the surface for the 17 cases summarized in Table 2.

note that there is a more direct correlation between the thickness of the small particle layer and the albedo (Fig. 12; lower right) in comparison with the radar echo-top height and albedo, which are not correlated below echo heights of 7 km.

We hypothesize that there is a link between the environmental thermodynamic structure and the micro-physical structure of convective systems. In cases of low CAPE, the convection extends to midlevels and the radar echo-top height and the IR equivalent height are virtually the same, suggesting that the radar observes the actual cloud top and that there is no layer of small ice particles above the larger particles. In cases of high CAPE, deep convective systems with connecting strat-

iform regions develop with much colder cloud tops that are higher than the radar echo tops. This region between the radar echo top and IR equivalent cloud-top height is likely to be occupied by populations of small ice crystals, which are an important contributor to the storm albedo. Observations from the TMI can be used to detect the presence of precipitation-sized ice particles. Nesbitt et al. (2000) examine the ice-scattering signature of precipitation at 85.5 GHz, using the polarization-corrected temperature (PCT) to define a threshold for the presence of ice precipitation. They define PCT < 250 K to indicate the presence of ice precipitation. For each of the cases we have identified as midlevel, the PCT is greater than 250 K over the entire storm with mean values greater than 280 K, indicating a lack of ice phase hydrometeors in the cloud. The deep convective cases each show PCT < 250 K for at least 10% of their area.

4. Sensitivity analysis

In order to test the sensitivity of our results to the parameters in the set of Z–I/LWC relations, we compare the modeled TOA upwelling fluxes with those measured by the CERES instrument for the 20 June 1998 case over a set of 26 different combinations of parameterizations and assumptions for the IWC and LWC and an additional 4 combinations for the 8 February 1998 case. Table 3 summarizes the different parameterizations used in the cloud top, large ice particle, and rain regions of the storm for each run. For the first five runs, the IWC and particle sizes for the cloud-top small-particle regime (IR equivalent cloud-top height $> z >$ radar echo height) are varied, holding all other parameters constant. The ranges of IWC for this region are taken from the results presented in Fig. 6 and represent fits to the extreme IWC values at the highest and lowest temperatures. The profile of particle sizes has been taken to range between the extremes of the particle size being constant with temperature at the largest and then the smallest size. In runs 6–11, the parameters of the Z–IWC relationship and the mean particle sizes are varied for radar range gates where $z >$ freezing level and dBZ_e < 29. The range of parameters for the Z–IWC relationship represents conservative bounds to the regression fits of Z_i versus IWC from Jensen et al. (2002) for island-based tropical anvil systems observed during MCTEX. Runs 12–18 examine the sensitivity to the parameters of the Marshall–Palmer (1948) distribution. The range of these parameters is taken to represent the range of some classic Z–R relationships summarized by Sauvageot (1992), including relationships derived for stratiform (Marshall and Palmer 1948), thunderstorm (Sekhon and Srivastava 1971), and snow (Sekhon and Srivastava 1970) precipitation. The assumption of an upper limit to the IWC is tested in runs 19–21 by extending the parameterization for dBZ_e < 29 to higher reflectivities. Runs 22–23 are control runs in which hydrometeor contents in various categories are set to zero

in order to investigate the contributions to the shortwave albedo in different particle sizes. Runs 24 and 25 test the sensitivity to the calculation of single-scattering properties in the radiative transfer model. Run 24 uses Mie theory to calculate the asymmetry parameter, while run 25 uses the parameterization of single-scattering properties of ice crystals developed by Fu and Liou (1993). Run 26 extends the freezing level to −35°C, investigating the sensitivity to the transition from liquid to ice. Runs 27–30 vary the mean particle size below the freezing level for the 9 February 1998 case. If we assume that the total LWC is dominated by raindrops detected by the TRMM PR, then this set of tests approximates changing the fraction of the total LWC that is contributed by smaller hydrometeors.

Figure 13 shows mean differences (±1 standard deviation) between the modeled and measured fluxes for each of the 30 different variations of the sensitivity tests summarized in Table 3. These results show that for the 20 June 1998 case, reflected solar flux is not very sensitive to uncertainties in the number of large precipitation particles above or below the freezing level. Rather, these fluxes are most sensitive to changes in size and number concentration of the ice crystals near the top of the cloud, which are not detected by the TRMM PR. The difference between runs 4 and 5 represents approximately 30% of the total upwelling solar flux; however, the particle size parameters for these runs represent extreme unlikely profiles of particle sizes. Run 25 shows that the use of parameterizations by Fu and Liou (1993) for the single-scattering properties of ice crystals results in a rather modest difference in the mean upwelling flux in comparison with our baseline case ($\sim$17 W m^{-2}). Because the Fu and Liou (1993), and other parameterizations like it, make assumptions about the particle shapes and because in situ observations of ice crystals from similar type storms (McFarquhar and Heymsfield 1996) identify the majority ice particle shape as ''indeterminate,'' we have chosen to use the more general $g = 0.7$ as our baseline case.

The control runs present information on the relative importance of the small and large hydrometeors in determining the shortwave albedo. Run 22 removes the contribution of the large precipitation-sized particles detected by the TRMM PR and calculates the shortwave albedo assuming only the small particles between the radar echo-top height and the IR equivalent cloud-top height are present. The presence of the small particles accounts for all but 117 ± 95 W m^{-2} of the mean reflected shortwave radiation of 834 W m^{-2}. Run 23 removes this layer of small particles and models the cloud system using only those hydrometeors detected by the TRMM PR. The modeled shortwave flux is 276 ± 219 W m^{-2} lower than the measured upwelling flux. This indicates that both the large and small particles must be included to calculate the cloud albedo with any precision, the small particles seem to contribute more to the reflection of shortwave radiation than do

TABLE 3. Summary of the 30 different combinations of parameterization used in the sensitivity analysis of Fig. 11.

Case No.	$z >$ echo top and $z <$ IR cloud-top height	$z >$ freezing level and dbZ$_e$ < 29	$z >$ freezing level and dBZ$_e$ > 29	$z >$ freezing level
1	IWC = 0.0032T + 0.3112, D_m = Table 1	a = 0.001, b = 0.96, D_m = 200 μm	IWC = 2.5 g m^{-3}, D_m = 425 μm	a = 0.004, b = 0.55, D_m = 750 μm
2	IWC = 0.0059T + 0.4518, D_m = Table 1	Same as No. 1	Same as No. 1	Same as No. 1
3	IWC = 0.0017T + 0.209, D_m = Table 1	Same as No. 1	Same as No. 1	Same as No. 1
4	IWC = 0.0032T + 0.3112, D_m = 220 μm	Same as No. 1	Same as No. 1	Same as No. 1
5	IWC = 0.0032T + 0.3112, D_m = 30 μm	Same as No. 1	Same as No. 1	Same as No. 1
6	Same as No. 1	a = 0.003, b = 0.96, D_m = 200 μm	Same as No. 1	Same as No. 1
7	Same as No. 1	a = 0.001, b = 0.25, D_m = 200 μm	Same as No. 1	Same as No. 1
8	Same as No. 1	a = 0.001, b = 1.25, D_m = 200 μm	Same as No. 1	Same as No. 1
9	Same as No. 1	a = 0.001, b = 0.96, D_m = 50 μm	Same as No. 1	Same as No. 1
10	Same as No. 1	a = 0.001, b = 0.96, D_m = 150 μm	Same as No. 1	Same as No. 1
11	Same as No. 1	a = 0.001, b = 0.96, D_m = 250 μm	Same as No. 1	Same as No. 1
12	Same as No. 1	Same as No. 1	Same as No. 1	a = 0.002, b = 0.55, D_m = 750 μm
13	Same as No. 1	Same as No. 1	Same as No. 1	a = 0.006, b = 0.55, D_m = 750 μm
14	Same as No. 1	Same as No. 1	Same as No. 1	a = 0.004, b = 0.45, D_m = 750 μm
15	Same as No. 1	Same as No. 1	Same as No. 1	a = 0.004, b = 0.65, D_m = 750 μm
16	Same as No. 1	Same as No. 1	Same as No. 1	a = 0.006, b = 0.55, D_m = 500 μm
17	Same as No. 1	Same as No. 1	Same as No. 1	a = 0.006, b = 0.55, D_m = 250 μm
18	Same as No. 1	Same as No. 1	Same as No. 1	a = 0.006, b = 0.55, D_m = 100 μm
19	Same as No. 1	Same as No. 1	a = 0.01, b = 0.96, D_m = 425 μm	Same as No. 1
20	Same as No. 1	Same as No. 1	a = 0.01, b = 0.96, D_m = 200 μm	Same as No. 1
21	Same as No. 1	None	Same as No. 1	None
22	Same as No. 1	None	None	None
23	None	Same as No. 1	Same as No. 1	Same as No. 1
24	Same as No. 1, but using Mie theory for single-scattering properties			
25	Same as No. 1, but using Fu and Liou (1993) parameterization for single-scattering properties			
26	Same as No. 1, but allowing liquid water to exist to −35°C			
	Model runs for 8 Feb 1998 case			
27	IWC = 0.0032T + 0.3112, D_m = Table 1	a = 0.001, b = 0.96, D_m = 200 μm	IWC = 2.5 g m^{-3}, D_m = 425 μm	a = 0.004, b = 0.55, D_m = 750 μm
28	Same as No. 26	Same as No. 26	Same as No. 26	a = 0.006, b = 0.55, D_m = 500 μm
29	Same as No. 26	Same as No. 26	Same as No. 26	a = 0.006, b = 0.55, D_m = 250 μm
30	Same as No. 26	Same as No. 26	Same as No. 26	a = 0.006, b = 0.55, D_m = 100 μm

the large particles; however, the difference is not outside the bounds of the variation within the cloud system. This seems to support the results of McFarquhar and Heymsfield (1997) who conclude from observations of anvils in different parts of the tropical Pacific that the large precipitation particles in the lower parts of tropical cirrus anvils are equally important to the small ice crystals near cloud top in producing high shortwave albedos.

Runs 26–29 indicate that for the midlevel cases, our results are rather sensitive to the portion of the LWC contributed by small cloud droplets. This is not an unexpected result and suggests the importance of understanding the contributions of cloud and precipitation
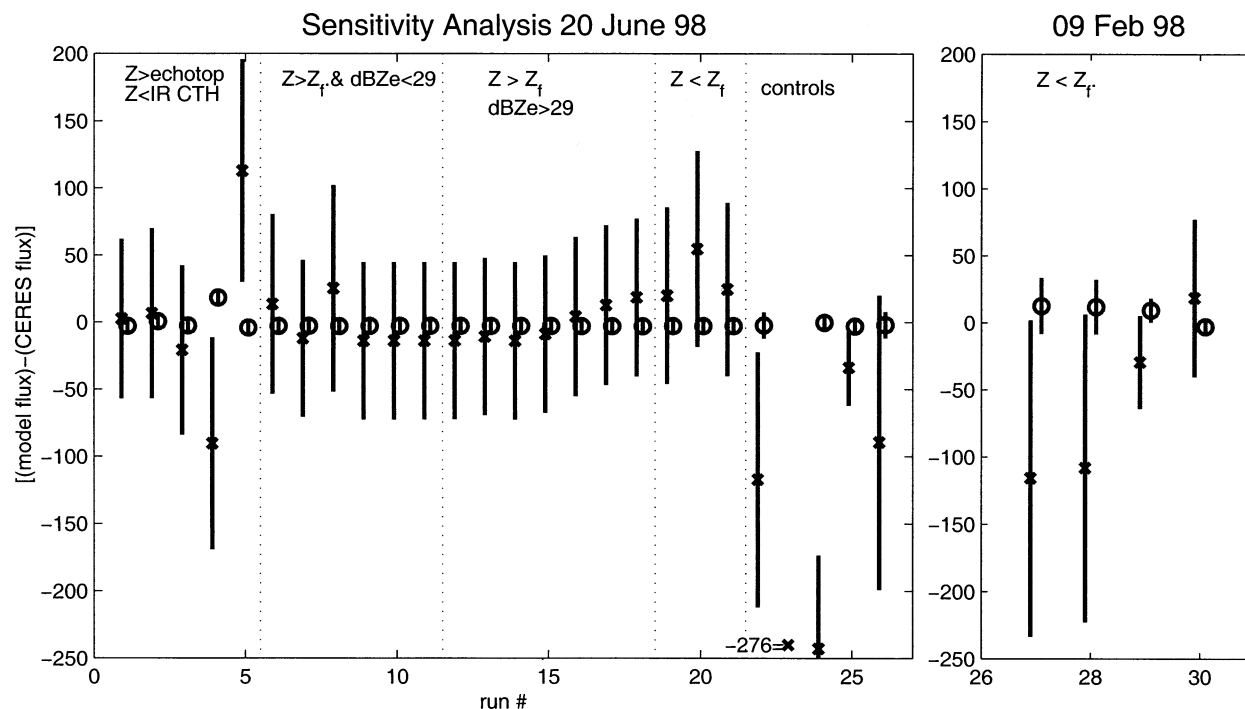
FIG. 13. Modeled TOA upwelling flux − CERES-measured TOA upwelling flux (solar = X, IR = O) for a set of 30 different combinations of parameterizations and assumptions for ice water content for the 0259 UTC 20 Jun 1998 deep convective case. The X/O represent the mean of this difference over all raining pixels. The bar represents ±1 standard deviation.

particles to the total liquid water content if we are to improve the description of radiative transfer calculations in these clouds.

5. Heating rates

The results of the radiative transfer calculations show reasonable agreement with measurements at the TOA and at the surface. Although this is a necessary condition for proving the accuracy of the derived cloud properties, it is not sufficient to determine a unique or necessarily correct cloud property profile. From the model results, we can only conclude that the parameterized cloud properties are consistent with the measured radiative fluxes. With this caveat in mind, we calculate radiative heating rate profiles implied by the hydrometeor distributions associated with our baseline parameter settings.

Figures 14a–b shows the storm-averaged shortwave and longwave heating rates for a midlevel convective (980209) and a deep convective case (980620). Only pixels with TRMM radar-observed precipitation are included in the average. These cases are chosen for illustration because they are the examples nearest local noon and, therefore, have the greatest impacts on the solar energy budget. The midlevel convective case has a maximum longwave cooling of ~9.5 K day^{-1}, and a maximum solar heating of ~4 K day^{-1} at the freezing level (~5 km), just below the mean IR equivalent cloud-top height (5.6 km). The deep convective case shows

larger shortwave heating and longwave cooling higher in the atmosphere associated with cloud top in comparison with the midlevel convection. The mean cloud-top longwave cooling is 14.1 K day^{-1} and mean cloud-top shortwave heating is 14.6 K day^{-1} at a height of ~14 km, such that there is a net radiative heating near cloud top. At cloud base there is also a net radiative heating with longwave heating on the order of 7.5 K day^{-1}. The large difference in radiative heating profiles in the deep and midlevel convective cases is the result of a difference in cloud-top height and a difference in cloud optical depth. Mean shortwave optical depths for the deep convective cases range between $\tau = 54$ and $\tau = 99$, while for midlevel convective cases $21 < \tau < 31$. The net effect of the dipole pattern of heating/cooling in the midlevel convection is to radiatively destabilize the cloud-top region. For the deep convective cases, on the other hand, the bimodal net heating pattern destabilizes both the cloud top and anvil base while stabilizing the interior of the anvil.

The sensitivity analysis in Fig. 12 shows that there is a relatively small change in the modeled upwelling shortwave flux at the TOA when the single-scattering properties are changed from $g = 0.7$ to the parameterizations of Fu and Liou (1993). However, Fig. 14c shows that there is a sensitivity to the shape of the shortwave heating rate profile. When using the parameterization from Fu and Liou (1993), the maximum heating rate is
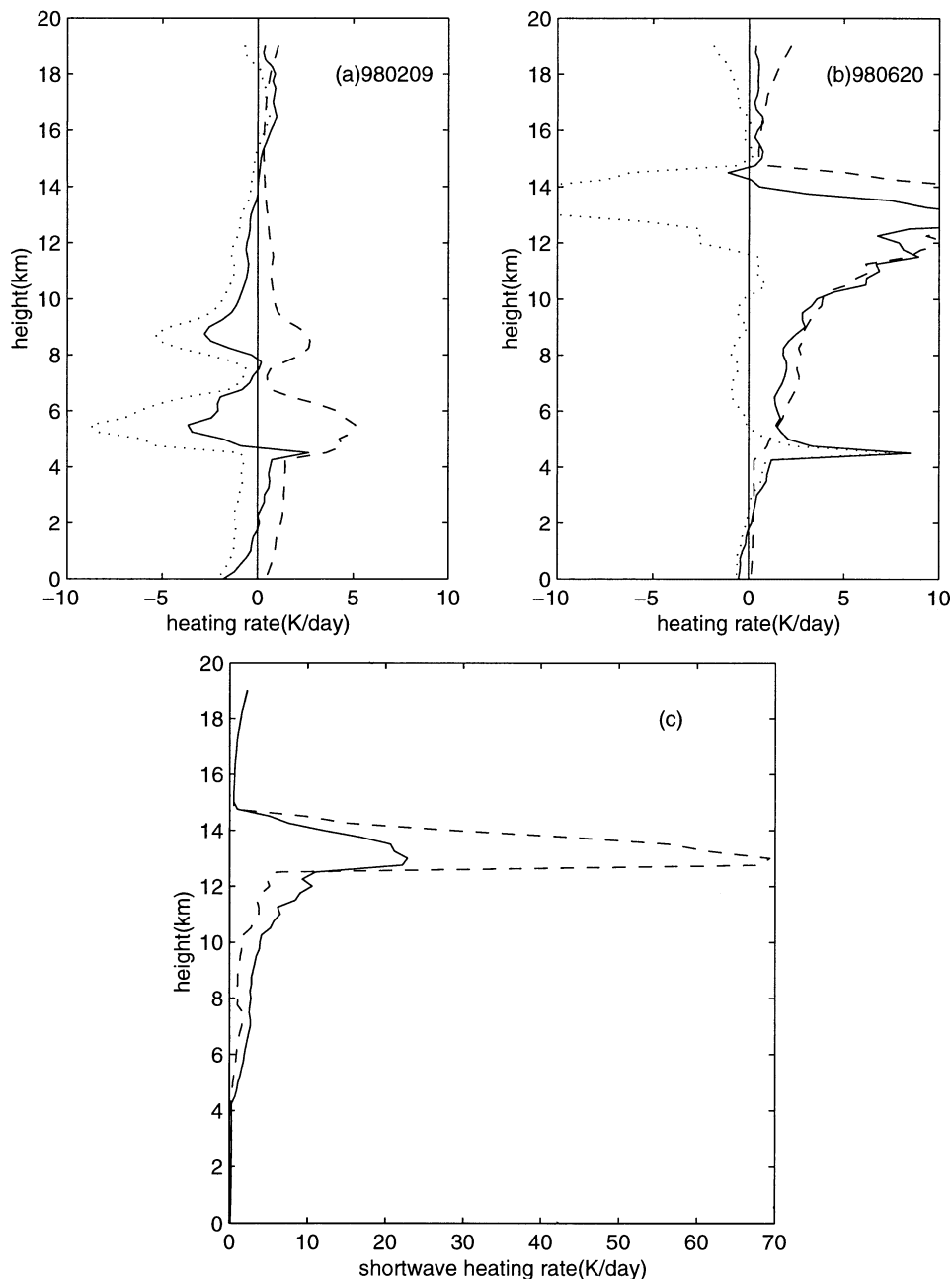
FIG. 14. Modeled shortwave (dashed), longwave (dotted), and total (solid) radiative heating for (a) a midlevel convection case at 2225 UTC 9 Feb 1998 and (b) a deep convective case at 0259 UTC 20 Jun 1998. (c) Modeled shortwave radiative heating for 0259 UTC 20 Jun 1998 using asymmetry parameter of 0.7 (solid) and using the parameterizations of Fu and Liou (1993) (dashed).

increased threefold. In reality, the true heating rate profile probably lies between these two curves.

The radiative flux convergence represents the radiative energy deposited into the atmospheric column and can be calculated using the equation

$$F_{net} = (F_{down} - F_{up})_{TOA} - (F_{up} - F_{down})_{sfc}.$$

For clear skies, there is a net divergence of longwave radiation representing a net cooling of the atmospheric column to space. For the 17 cases investigated in this study, the clear-sky longwave flux convergence ranges between -310 and -280 W m^{-2}. The presence of a cloud in the atmospheric column will generally result in a decrease in the upwelling longwave flux at the TOA and an increase in the downwelling longwave flux at the surface. Because the water vapor content is very high in the lower tropical atmosphere, longwave optical depth is already very large, and the addition of cloud

particles has only a minor effect on the emitting temperature of the lower atmosphere. The net result is a decrease in the longwave cooling of the atmospheric column. There is a distinct difference between the radiative flux convergence of deep convection and that of midlevel convection. For the midlevel convective cases, the mean longwave flux convergence ranges from -202 to 212 W m^{-2}. For the deep convective cases, the longwave flux convergence ranges between -60 and -137 W m^{-2}. The longwave radiative cooling is greatly reduced because of the low-emission temperature of the anvil cloud tops.

The comparison of the shortwave flux convergence is complicated by a much more pronounced diurnal cycle with the greatest deposition of energy at local solar noon. The shortwave flux convergence ranges between 167 and 242 W m^{-2} for the midlevel convection and between 46 and 287 W m^{-2} for the deep convective cases. However, if we normalize the flux convergence by dividing by the downwelling shortwave flux at the surface for clear-sky conditions, we find that the shortwave flux convergence, or the shortwave flux deposited into the atmospheric column, is equal to 20%–32% of the clear-sky flux at the surface for both deep and midlevel convective cases. Therefore, increasing convection depth implies decreasing net radiative cooling of the atmosphere.

To evaluate the relative importance of radiative heating in tropical anvils compared to latent heating, we can compare the calculated radiative heating rate profiles with studies of the large-scale apparent heat source Q_1 for tropical convective systems. Here, Q_1 is the sum of the latent heating, radiative heating, and eddy flux transports of heat and moisture (Yanai et al. 1973). The stratiform region of a tropical mesoscale convective system is characterized by heating due to condensation above the freezing level and cooling due to melting and evaporating below the freezing level, while the convective region shows heating by condensation through the depth of the troposphere (Houze 1989). Lin and Johnson (1996) diagnostically determine profiles of Q_1 for convective systems observed during the Tropical Ocean and Global Atmosphere Coupled Ocean–Atmosphere Response Experiment (TOGA COARE). They show positive latent heating through the depth of the troposphere with a single maximum of ~ 30 K day^{-1} at a height of 7–8 km. A comparison of this profile with Figs. 14a and 14b shows that, for deep convective cases, the net radiative heating maximum is located higher in the atmosphere than the peak Q_1 but is of a magnitude of 70%–90% less than the total Q_1. Therefore, near solar noon, the radiative heating in deep convective anvils may contribute as much as 30% of the total Q_1. If this comparison were to be repeated using the parameterization of ice crystal single-scattering properties from Fu and Liou (1993), Fig. 14c, the relative importance of the radiative heating in comparison with latent heating would be even larger.

6. Conclusions

The broadband radiative characteristics for a total of 17 precipitating regions observed by the TRMM satellite over the Manus or Nauru Island ARM sites were modeled. These cases represent both deep convective and midlevel convective cases. We are able to model the TOA and surface broadband radiative fluxes to within 10%–20% of the values observed by CERES over the precipitating regions of deep convective systems. These modeled fluxes are most sensitive to the choice of cloud particle sizes below the detectability threshold of the TRMM PR and are relatively insensitive to the parameters of the Z–IWC relationships describing the large hydrometeors in the precipitating regions of the cloud.

The results suggest a relationship among the environmental thermodynamics, the probable cloud microphysics, and the cloud radiative forcing. When environmental CAPE is large, there is the opportunity for deep convective clouds with extended anvil decks containing deep layers with small ice crystals with large optical thickness to form. This results in shortwave heating and longwave cooling associated with cloud top at heights of 12–14 km. When environmental CAPE is small, convective clouds extend only to midlevels (4–7 km) and do not develop a deep layer of small ice crystals. Cloud-top radiative heating and cooling in these cases is maximum near the freezing level. If this relationship between environmental thermodynamics and cloud forcing by convective clouds is found to be consistent in a statistically significant number of cases, the environmental CAPE may be useful as a constraint on the upper limit of cloud forcing by convective clouds in the Tropics.

Our investigation of the sensitivity of the modeled shortwave albedo to different combinations of the parameterized cloud microphysics showed that our results are most sensitive to the prescribed sizes of cloud ice below the detectability threshold of the TRMM PR. The control runs of our sensitivity analysis suggest that in order to explain the high albedos of these tropical deep convective we must include both the large precipitation particles that are detected by the TRMM PR and the smaller ice particles near cloud top that go undetected. This seems to support the findings of McFarquhar and Heymsfield (1997), who placed equal significance in the production of high albedos on the large particles in the lower regions of the cloud.

The description of the energetics associated with deep convective anvil systems is often considered to be dominated by latent heating effects, such that the radiative impacts of these systems are neglected or considered to be equivalent to a tropical clear- or all-sky mean value. A comparison of the radiative heating profiles calculated in this study with latent heating profiles from previous studies shows that, for cases of mature deep convection near local solar noon, the maximum radiative heating

is on the order of 10%–30% of the maximum latent heating in deep convective storms. However, the maximum radiative heating is generally located higher in the atmosphere, near cloud top, in comparison with the maximum latent heating and also produces an additional maximum near anvil base. Therefore, studies of the energetics or dynamics of tropical anvils must take into account the role of radiative processes.

REFERENCES

Ackerman, T. P., K. Liou, F. P. J. Valero, and L. Pfister, 1988: Heating rates in tropical anvils. *J. Atmos. Sci.,* **45,** 1606–1623.

Cahalan, R. F., W. Ridgeway, W. J. Wiscombe, T. L. Bell, and J. B. Snider, 1994: The albedo of fractal stratocumulus clouds. *J. Atmos. Sci.,* **51,** 2434–2455.

Christian, H. J., R. J. Blakeslee, and S. J. Goodman, 1999: Lightning Imaging Sensor (LIS) for the Earth Observing System. NASA Tech. Memo. TM-4350, 44 pp. [Available from Center for Aerospace Information, P. O. Box 8757, Baltimore–Washington International Airport, Baltimore, MD 21240.]

Churchill, D. D., 1992: Vertical retrieval of solar and infrared irradiances in the stratiform regions of EMEX cloud clusters. *J. Appl. Meteor.,* **31,** 1229–1247.

Del Genio, A. D., and W. Kovari, 2002: Climatic properties of tropical precipitating convection under varying environmental conditions. *J. Climate,* **15,** 2597–2615.

Francis, P. N., A. Jones, R. W. Saunders, K. P. Shine, A. Slingo, and Z. Sun, 1994: An observational and theoretical study of the radiative properties of cirrus: Some results from ICE '89. *Quart. J. Roy. Meteor. Soc.,* **120,** 809–848.

Fu, Q., and K. N. Liou, 1993: Parameterization of the radiative properties of cirrus clouds. *J. Atmos. Sci.,* **50,** 2008–2025.

Hartmann, D. L., H. H. Hendon, and R. A. Houze Jr., 1984: Some implications of the mesoscale circulations in tropical cloud clusters for large-scale dynamics and climate. *J. Atmos. Sci.,* **41,** 113–121.

Heymsfield, A. J., and A. G. Palmer, 1986: Relationships for deriving thunderstorm anvil ice mass for CCOPE storm water budget estimates. *J. Appl. Meteor.,* **25,** 691–702.

——, and G. M. McFarquhar, 1996: High albedos of cirrus in the tropical Pacific warm pool: Microphysical interpretations from CEPEX and from Kwajalein, Marshall Islands. *J. Atmos. Sci.,* **53,** 2424–2450.

Houze, R. A., Jr., 1989: Observed structure of mesoscale convective systems and implications for large-scale heating. *Quart. J. Roy. Meteor. Soc.,* **115,** 425–461.

Jensen, M. P., T. P. Ackerman, and S. M. Sekelsky, 2002: Radiative impacts of anvil cloud during the Maritime Continent Thunderstorm Experiment. *J. Appl. Meteor.,* **41,** 473–487.

Kato, S., T. P. Ackerman, J. H. Mather, and E. E. Clothiaux, 1999: The *k*-distribution method and correlated-*k* approximation for a shortwave radiative transfer model. *J. Quant. Spectrosc. Radiat. Transfer,* **62,** 109–121.

Kummerow, C., W. Barnes, T. Kozu, J. Shiue, and J. Simpson, 1998: The Tropical Rainfall Measuring Mission (TRMM) sensor package. *J. Atmos. Oceanic Technol.,* **15,** 809–817.

Lin, X., and R. H. Johnson, 1996: Heating, moistening, and rainfall over the western Pacific during TOGA COARE. *J. Atmos. Sci.,* **53,** 3367–3383.

Lindzen, R. S., M. Chou, and A. Y. Hou, 2001: Does the earth have an adaptive infrared iris? *Bull. Amer. Meteor. Soc.,* **82,** 417–432.

Marshall, J. S., and W. M. K. Palmer, 1948: The distribution of raindrops with size. *J. Meteor.,* **5,** 165–166.

Mather, J. H., T. P. Ackerman, W. E. Clements, F. J. Barnes, M. D. Ivey, L. D. Hatfield, and R. M. Reynolds, 1998: An atmospheric radiation and cloud station in the tropical western Pacific. *Bull. Amer. Meteor. Soc.,* **79,** 627–642.

McFarquhar, G. M., and A. J. Heymsfield, 1996: Microphysical characteristics of three anvils sampled during the Central Equatorial Pacific Experiment. *J. Atmos. Sci.,* **53,** 2401–2423.

——, and ——, 1997: Parameterization of tropical cirrus ice crystal size distributions and implications for radiative transfer: Results from CEPEX. *J. Atmos. Sci.,* **54,** 2187–2200.

Moncrieff, M. W., and J. S. A. Green, 1972: The propagation and transfer properties of steady convective overturning in shear. *Quart. J. Roy. Meteor. Soc.,* **98,** 336–352.

Nesbitt, S. W., E. J. Zipser, and D. J. Cecil, 2000: A census of precipitation features in the Tropics using TRMM: Radar, ice scattering, and lightning observations. *J. Climate,* **13,** 4087–4106.

Ramanathan, V., and W. Collins, 1991: Thermodynamic regulation of ocean warming by cirrus clouds deduced from observations of the 1987 El Niño. *Nature,* **351,** 27–32.

Sassen, K., 1987: Ice cloud content from radar reflectivity. *J. Climate Appl. Meteor.,* **26,** 1050–1053.

Sauvageot, H., 1992: *Radar Meteorology.* Artech House, 366 pp.

Sekhon, R. S., and R. C. Srivastava, 1970: Snow size spectra and radar reflectivity. *J. Atmos. Sci.,* **27,** 299–307.

——, and ——, 1971: Doppler radar observations of drop-size distribution in a thunderstorm. *J. Atmos. Sci.,* **28,** 983–994.

Smith, P. L., 1984: Equivalent radar reflectivity factors for snow and ice particles. *J. Climate Appl. Meteor.,* **23,** 1258–1260.

Stephens, G. L., S.-C. Tsay, P. W. Stackhouse, and P. J. Flatau, 1990: The relevance of the microphysical and radiative properties of cirrus clouds to climate and climatic feedback. *J. Atmos. Sci.,* **47,** 1742–1753.

Stokes, G. M., and S. E. Schwartz, 1994: The Atmospheric Radiation Measurement (ARM) Program: Programmatic background and design of the Cloud and Radiation Test Bed. *Bull. Amer. Meteor. Soc.,* **75,** 1201–1221.

Toon, O. B., C. P. McKay, T. P. Ackerman, and K. Santhanam, 1989: Rapid calculation of radiative heating rates and photodissociation rates in inhomogeneous multiple scattering atmospheres. *J. Geophys. Res.,* **94,** 16 287–16 301.

Wielicki, B. A., B. R. Barkstrom, E. F. Harrison, R. B. Lee III, G. L. Smith, and J. E. Cooper, 1996: Clouds and the Earth's Radiant Energy System (CERES): An Earth Observing System Experiment. *Bull. Amer. Meteor. Soc.,* **77,** 853–868.

Yanai, M., S. Esbensen, and J. Chu, 1973: Determination of average bulk properties of tropical cloud clusters from large-scale heat and moisture budgets. *J. Atmos. Sci.,* **30,** 611–627.